Journal of Geophysical Research: Oceans

RESEARCH ARTICLE
10.1029/2018JC014081

Decadal Variability of Eddy Characteristics and Energetics in the Kuroshio Extension: Unstable Versus Stable States

Haiyuan Yang[1], Bo Qiu[1,2], Ping Chang[1,3], Lixin Wu[1], Shengpeng Wang[1], Zhaohui Chen[1], and Yun Yang[4]

[1]Physical Oceanography Laboratory, Ocean University of China and Pilot National Laboratory for Marine Science and Technology, Qingdao, China, [2]Department of Oceanography, University of Hawaii at Manoa, Honolulu, HI, USA, [3]Department of Oceanography and Department of Atmospheric Sciences, Texas A&M University, College Station, College Station, TX, USA, [4]College of Global Change and Earth System Science, Beijing Normal University, Beijing, China

Key Points:
- Energy-weighted length scale of eddies in the KE region is about 250 km; in the upstream (downstream) region, eddies tend to be stretched in the zonal (meridional) direction
- In the upstream, the unstable state is characterized by strong eddy-shedding processes; strong cyclonic eddies are found to be pinched off from the first quasi-stationary meander and are controlled by both baroclinic and barotropic instabilities
- In the downstream, eddy activity is mainly regulated by the upstream through lateral advection

Correspondence to:
H. Yang,
yanghaiyuan@ouc.edu.cn

Citation:
Yang, H., Qiu, B., Chang, P., Wu, L., Wang, S., Chen, Z., & Yang, Y. (2018). Decadal variability of eddy characteristics and energetics in the Kuroshio Extension: Unstable versus stable states. *Journal of Geophysical Research: Oceans*, *123*. https://doi.org/10.1029/2018JC014081

Received 14 APR 2018
Accepted 27 AUG 2018
Accepted article online 4 SEP 2018

Abstract Using the Estimating Circulation and Climate of the Ocean Phase II product, this study investigates the eddy characteristics and energetics in two dynamical regimes within the Kuroshio Extension (KE) region. Based on the empirical orthogonal function analysis, it is found that the decadal evolution of eddy kinetic energy in the KE region is characterized by a delayed negative correlation between the upstream and downstream. Besides the out-of-phase change in eddy activity levels, eddy characteristics and energetics in the upstream KE are also different from those in the downstream. In the upstream region, eddies are stretched in the zonal direction and the unstable state is characterized by strong eddy-shedding processes. During these processes, cyclonic eddies are found to be formed in the first quasi-stationary meander and finally pinched off from the KE jet. Energy budget illustrates that the eddy shedding processes are triggered by baroclinic instability, while barotropic instability becomes the dominated energy source after the meander is fully developed. Accompanied by the generation of cyclonic eddies, significant inverse energy cascade is detected. When the upstream KE is stable, the eddy activity is dominated by baroclinic instability and the inverse energy cascade occurs similarly. Distinct from the upstream, eddies in the downstream KE tend to be stretched in the meridional direction and the decadal variability of eddy kinetic energy in this region is mainly regulated by the upstream through lateral advection.

Plain Language Summary Based on classic physical oceanography theory, oceanic eddies are generated mainly through the vertical shear of background mean flow, i.e. baroclinic instability (BC). A stronger mean flow should favor BC and lead to more eddy generation. However, at decadal timescales, the correlation between the strength of the Kuroshio Extension (KE) jet and the regional eddy kinetic energy (EKE) level is negative, therefore the decadal variability of mesoscale eddy field in the KE system cannot be simply explained by the classic instability theory. This study explores in great depth the dynamical processes in the unstable state in the upstream KE and analyzes the evolution of eddy energetics during these processes. It is found that unstable events in the upstream KE are characterized by strong eddy-shedding processes. During these events, cyclonic eddies are found to be formed in the first quasi-stationary meander and finally pinched off from the KE jet. During these processes, both BC and barotropic energy transfer are important in the generation of eddies. This study will be a step toward the understanding of low-frequency variability in strong oceanic current regions in the global ocean.

1. Introduction

The Kuroshio Extension (KE) is the western boundary current extension of the subtropical gyre in the North Pacific Ocean after the Kuroshio separates from the coast of Japan. As an intense inertial jet, the KE is characterized by large-amplitude meanders and energetic pinched-off eddies (e.g., Joyce et al., 2001; Kida et al., 2015; Nakano et al., 2013; Qiu et al., 1991; Sasaki & Minobe, 2015; Figure 1). Based on the satellite altimeter measurement of the past 25 years, it is found that the level of eddy kinetic energy (EKE) undergoes a well-defined decadal variation, which reflects the decadal fluctuations of the KE system between a stable and an unstable dynamic state (e.g., Ceballos et al., 2009; Kelly et al., 2010; Qiu & Chen, 2005, 2010; Sasaki et al., 2013; Sugimoto & Hanawa, 2009; Taguchi et al., 2007, 2010). When the KE jet is in the stable state, its along-jet transport tends to be greater, and the EKE level in the upstream (downstream) KE region tends

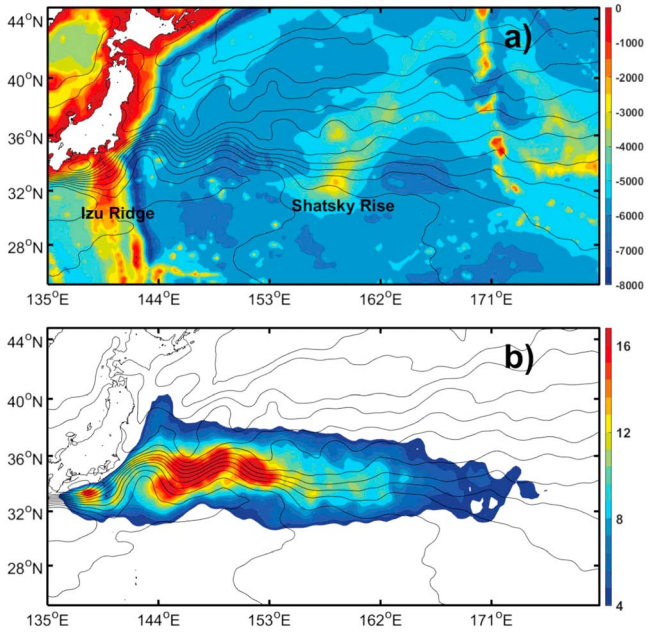

Figure 1. (a) Mean bathymetry (colored shading; m) based on Estimating the Circulation and Climate of the Ocean, Phase II (ECCO2) in the western North Pacific. (b) Mean eddy kinetic energy (EKE) field during 1993–2015 based on Archiving, Validation, and Interpretation of Satellite Oceanographic (AVISO) data set (colored shading; 0.01 m^2/s^2). The EKE is defined based on equation (1). Contours denote mean SSH field during 1993–2015 based on AVISO.

to decrease (increase). The reverse is true when the KE jet changes to the unstable dynamic state. To date, this decadal variability has been emphasized by several studies to be important for the basin-scale climate and marine ecosystems in the North Pacific (Bishop, 2013; Kida et al., 2015; Kwon et al., 2010; Qiu et al., 2014; Qiu & Chen, 2011).

Potential causes for the KE decadal variability have been proposed in many previous studies and can be divided into two categories: external-forcing and internal-forcing theories. The external-forcing theory conjectures that oceanic variability in the KE region is primarily a response to westward propagating baroclinic long Rossby waves from the central North Pacific forced by atmospheric anomalies associated with the Pacific Decadal Oscillation or North Pacific Gyre Oscillation (Deser et al., 1999; Miller et al., 1998; Qiu, 2003; Qiu et al., 2007, 2014; Sasaki & Schneider, 2011; Taguchi et al., 2005, 2007). In contrast, the internal-forcing theory hypothesizes that decadal evolution in the KE region can be understood through bifurcation of nonlinear dynamical systems (Berloff et al., 2007; Dijkstra & Ghil, 2005; Hogg et al., 2005; Jiang et al., 1995; McCalpin & Haidvogel, 1996; Primeau & Newman, 2008; Pierini, 2014; Pierini et al., 2009; Sun et al., 2013). According to this theory, the transition between the two well-defined states of EKE level is achieved by internal nonlinear processes within the ocean such as advection, flow instability, and eddy-mean flow interaction. In addition to these mechanisms, Qiu and Chen (2005) suggested a possible interaction between the decadal-shifting KE jet and the Izu-Ogasawara Ridge (Figure 1a). When the incoming negative (positive) sea surface height (SSH) anomaly generated in the central North Pacific reach 140°E southeast of Japan, the inflow KE is forced southward (northward) and runs into the shallow (deep) portion of the ridge, leading to strong (weak) eddy activity in the upstream KE region.

In addition to the processes that drive the decadal variability of EKE in the KE region, eddy energetics during the evolution, especially the energy sources, have also attracted much attention. During the past decades, BC has been considered to be the primary energy source for eddies in the global ocean (Bishop, 2013; Chen et al., 2014; Ferrari & Wunsch, 2009; Gill et al., 1974; Jia et al., 2011; Pedlosky, 1987; Penduff et al., 2004; Travis & Qiu, 2017). According to the BC theory, eddies draw their energy from the release of available potential energy stored in the large-scale circulation built up by the wind-driven Ekman pumping/suction. In the KE region, Bishop (2013) reported that generation of deep eddies is consistent with the BC scenario based on in situ observations. However, at decadal timescales, the negative correlation between the strength of the KE jet and the regional EKE level is rather counterintuitive. Since the stability analysis commonly suggests that a stronger mean flow should favor BC and lead to more eddy generation, the decadal variability of mesoscale eddy field in the KE system cannot be simply explained by the classic instability theory. Based on both observations and an idealized model study, Waterman and Jayne (2011) and Waterman et al. (2011) indicated that the KE jet is subject to a mixed instability mechanism. Using a multiscale energy and vorticity analysis method, Yang and Liang (2016) and Yang et al. (2017) suggested the important role of barotropic instability (BT) in the eddy energy budget within the KE region. They claimed that both BT and BC are important for the growth of EKE in the time-mean sense, while the decadal modulation of EKE is mainly controlled by BT. In the high-EKE state, an efficient barotropic energy transfer from mean flow to eddies is caused by the strong horizontal shear of large-amplitude meanders. In contrast, BC is responsible for the eddy energy generation in the low-EKE state.

While these previous studies have significantly improved our knowledge of the decadal variability of the eddy fields in the KE region, some important issues remain unsolved. First, eddy characteristics that determine the evolution of EKE level and its interaction with the mean flow, such as the energy length scales (Qiu et al., 2008; Wang et al., 2015) and eddy shapes (Waterman & Hoskins, 2013), are not fully studied. Second, because of lack of detailed descriptions in the existing literatures, our understanding about the dynamic processes during the unstable period, especially in the upstream KE, remains fragmentary. Third,

and perhaps most importantly, the dominant energy source of eddy generation during the decadal modulation, especially how eddies obtain more energy from a relative weak background flow during the unstable state, is still not fully quantified. These issues pose hindrances to our understanding of the potential mechanisms that control the decadal KE variability.

In this paper, the above mentioned issues regarding the decadal variability of EKE in the KE region are examined through analyzing an eddy-permitting global ocean state estimate. Here we will focus on the dynamics during the unstable and stable states of the KE separately. The rest of this paper is organized as follows: Section 2 gives a brief description of the data used in this study. In section 3, a detailed study of the eddy characteristics when the KE is stable and unstable is presented, followed by the eddy energetics analysis in section 4. The paper ends with a summary and further discussion in section 5.

2. Data

2.1. Model Data

The data used in this study are Estimating the Circulation and Climate of the Ocean (ECCO), Phase II product (ECCO2, http://apdrc.soest.hawaii.edu/data/; cube 92 version), which is also used by Yang et al. (2017). It is based on the Massachusetts Institute of Technology General Circulation Model (MITgcm; Marshall et al., 1997). The model solves the primitive equations in the global ocean on the cube-sphere grid (Adcroft et al., 2004). It has a horizontal resolution of 0.25° and 50 vertical levels with thicknesses varying from 10 m near the surface to 456 m near the bottom at a maximum depth of 6,150 m. Bottom topography is set based on Smith and Sandwell (1997). Quadratic drag law is applied to parameterize the bottom stress, while biharmonic friction is used in horizontal direction. The K-profile parameterization vertical mixing scheme from Large et al. (1994) is employed to parameterize subgrid-scale vertical mixing processes.

The eddy-permitting ECCO2 ocean state estimate is obtained by a least squares fit of the MITgcm to available satellite and in situ data. Using the Green function approach (Menemenlis et al., 2005), the least squares fit is applied for a number of control parameters (e.g., the initial condition, surface boundary conditions, background vertical viscosity, and bottom drag coefficient). With these optimized control parameters, the model is run forward freely without unphysical jumps and artificial sources/sinks. Thus, the solution is both realistic and dynamically consistent, which makes the solution useful for process and budget analyses (Wunsch et al., 2009). The ECCO2 state estimate has been used in the past to diagnose the eddy dynamics and oceanic energetics in the KE region (e.g., Chen et al., 2014; Yang et al., 2017). In this study, the 3-day-averaged data set in the KE region (140°E–180°E, 25°N–45°N) from 1993 to 2015 is used.

2.2. Satellite Observation

To validate the ECCO2 state estimate output in the region of our interest, the merged absolute dynamic topography (ADT) product derived from measurements of two satellites (TOPEX/Poseidon or Jason-1 and ERS or Envisat) is used in this study. The merged ADT data are distributed by Archiving, Validation, and Interpretation of Satellite Oceanographic data set (AVISO, http://www.aviso.oceanobs.com/) and are better than the data sets using a single altimeter in resolving the mesoscale spatial and temporal variability of the ocean circulation (Ducet et al., 2000; Le Traon & Dibarboure, 1999). The horizontal resolution of the ADT data set is 0.25° at daily intervals. Similar to the ECCO2 data, the concurrent SSH fields during 1993–2015 within the region (140°E–180°E, 25°N–45°N) are used in our analysis.

3. Eddy Characteristics

Before exploring the eddy characteristics and generation mechanism in the KE region, it is necessary to quantify whether ECCO2 can capture the decadal evolution of eddy fields as observed by satellite. By performing an empirical orthogonal function (EOF) analysis, we compare the dominant patterns of EKE variability derived from the ECCO2 and satellite observations. Here EKE is defined as

$$\mathrm{EKE} = \frac{1}{2}\left(u'^2 + v'^2\right), \tag{1}$$

where u' and v' denote zonal and meridional surface velocity deviation from their 270-day running-mean values. This definition is based on the eddy characteristic periods in the KE region suggested by previous

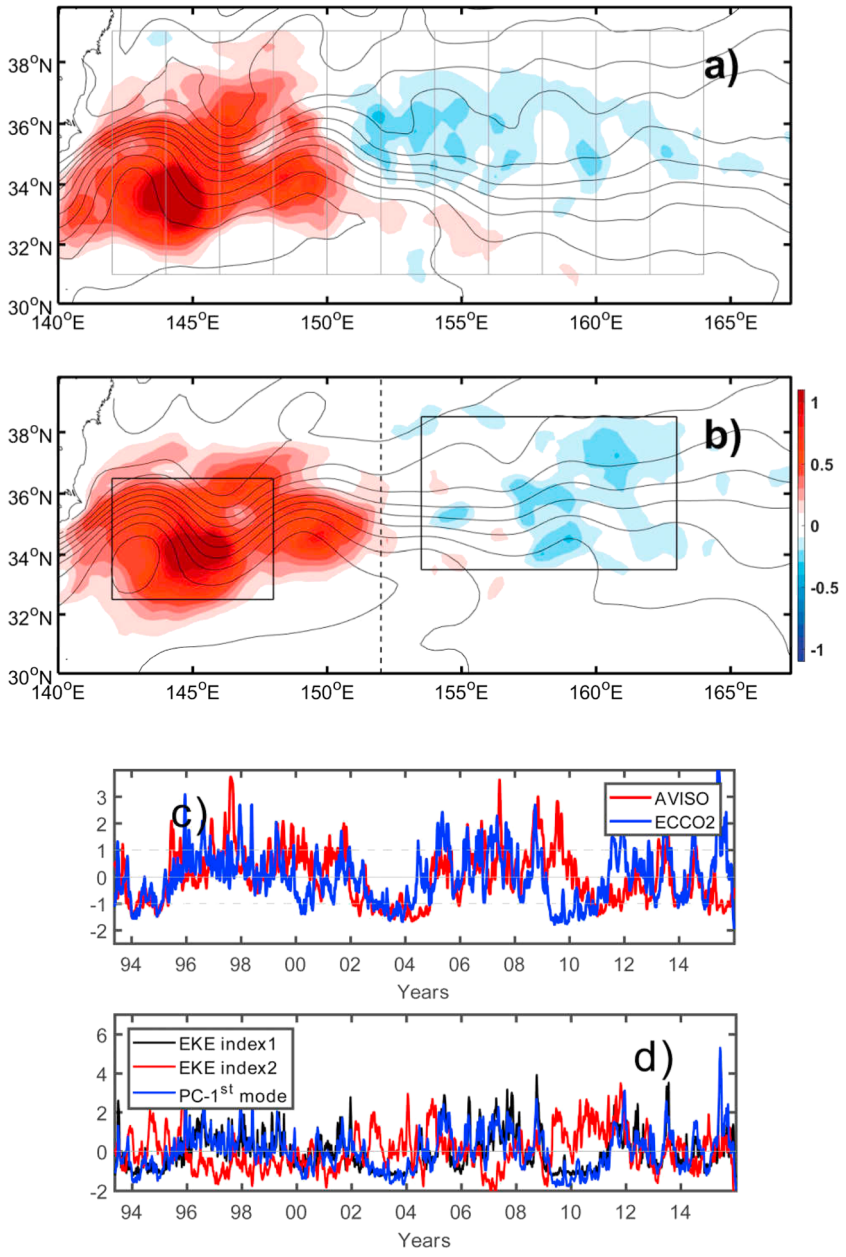

Figure 2. The first EOF mode of EKE during 1993–2015 (colored shading; 0.1 m^2/s^2) derived from (a) AVISO and (b) ECCO2. Contours denote mean SSH field during 1993–2015. The black dash line in (b) indicates 152°E. (c) Normalized PC of the first EOF mode derived from AVISO and ECCO2. (d) Time series of EKE index1, EKE index2, and PC of the first EOF mode from ECCO2.

studies (Itoh & Yasuda, 2010; Yang et al., 2017). Changing this running-mean window within the range of 180 to 400 days does not affect the following analysis results qualitatively. Figure 2 shows the first EOF modes obtained from ECCO2 and AVISO, which explain 7.7% and 6.3% (and are distinct from the second EOF according to the rule of North et al., 1982) of the total variance, respectively. The explained variances reach 25.1% and 28.2%, respectively, after applying a 1-year low-pass filter to the original EKE data. The pattern of the ECCO2 EOF mode resembles that from altimetry (cf. Figures 2a and 2b) and is characterized by a dipole pattern divided at 152°E with the largest amplitude located at the KE's first quasi-stationary meander (around 143°E–147°E, 33°N–35°N). In addition to their spatial consistency, comparison between the two principle components (PCs) reveals that both EOF modes are dominated by decadal modulations

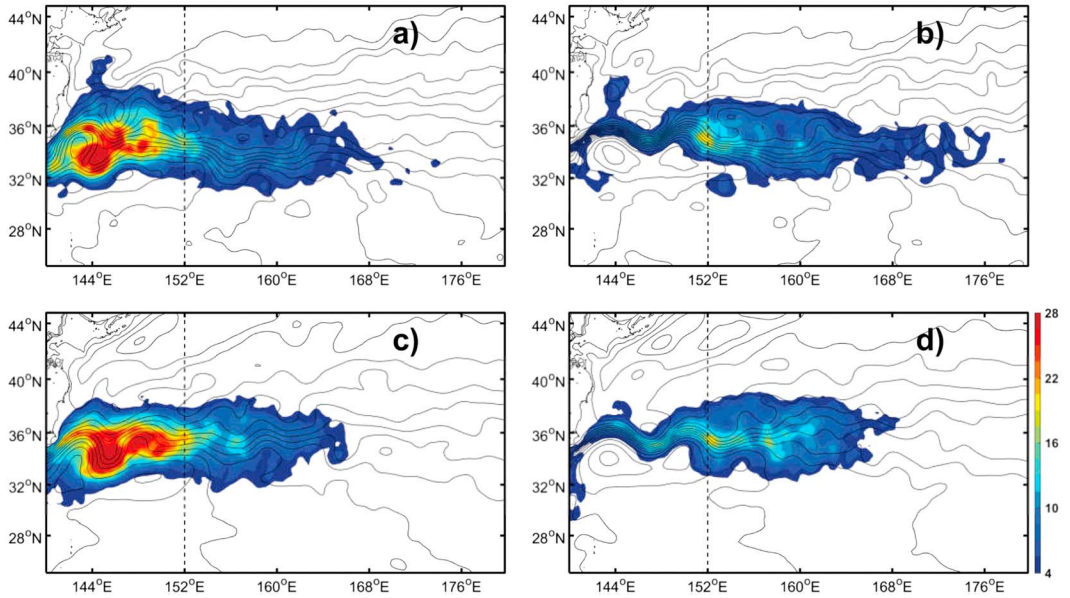

Figure 3. Mean EKE distribution (colored shading; 0.01 m^2/s^2) when KE is (a) unstable and (b) stable based on AVISO. Contours are state-mean SSH isolines. (c) and (d) are same as (a) and (b) but derived from ECCO2. The black dash lines indicate 152°E.

in which high (low) EKE level is found in 1996–1999 and 2007–2009 (1994–1995 and 2002–2004, Figure 2c). The correlation between these two PCs is 0.55 after applying the 1 year low-pass filter and is significant at the 95% confidence level (the degrees of freedom for the low-passed time series are evaluated based on the Monte Carlo test; hereinafter, all correlations are found to be significant at the 95%confidence level). This suggests that ECCO2 successfully simulates both the spatial and temporal evolutions of the eddy activity in the KE region. What is interesting from Figures 2a and 2b is that the decadal evolution of eddy activity has opposite signs in the upstream versus downstream regions. It implies that when the eddy activity is enhanced in the upstream region west of 152°E, the downstream EKE level east of 152°E tends to be reduced. This can be verified by comparing the normalized EKE time series (obtained by removing the time-mean value and divided by standard deviation) averaged in the upstream (142°E–148°E, 32.5°N–36.5°N; left box in Figure 2b) and downstream (153°E–164°E, 33.5°N–38.5°N; right box in Figure 2b) KE regions from ECCO2 (Figure 2d; hereinafter, these two series are referred to as EKE index1 and EKE index2, respectively). The linear correlation coefficient between these two 1 year-low-pass-filtered EKE time series reaches −0.66 when the upstream leads by about 300 days. In addition to the negative correlation between the upstream and downstream eddy activity levels, it is also revealed from Figures 2a and 2b that the EKE variability in the KE region is dominated by its upstream component, a feature that can also be inferred from the high correlation between the EKE index1 and PC of the first EOF mode (blue and black lines in Figure 2d).

The longitudinal EKE variation along the KE jet is further explored by employing the composite analysis. Based on normalized PC of the first EOF mode, two dynamical states of the KE jet are defined. The unstable state is given by the ensemble of flow states in which the normalized PC is larger than +1, while the stable state occurs when normalized PC is smaller than −1. According to this definition, 436 and 401 samples (about 1,300 and 1,200 days) are selected for the unstable and stable composites, respectively. Figure 3 shows the composite maps of EKE and SSH for the two dynamical states obtained from ECCO2 and AVISO, respectively. During the unstable period, energetic eddies occupy the upstream KE region with EKE maximum in the vicinity of the trough of meander (Figures 3a and 3c). In comparison, the eddy activity reduces significantly and is confined to the downstream in the stable state (Figures 3b and 3d). The decadal modulation of eddy activity is accompanied by the intensity changes of the KE jet and its southern recirculation gyre. Compared to the unstable state, the KE jet in the stable state is more intense (i.e., having a greater cross-stream SSH jump), extends more coherently eastward of 152°E, and is accompanied by the presence of a better defined

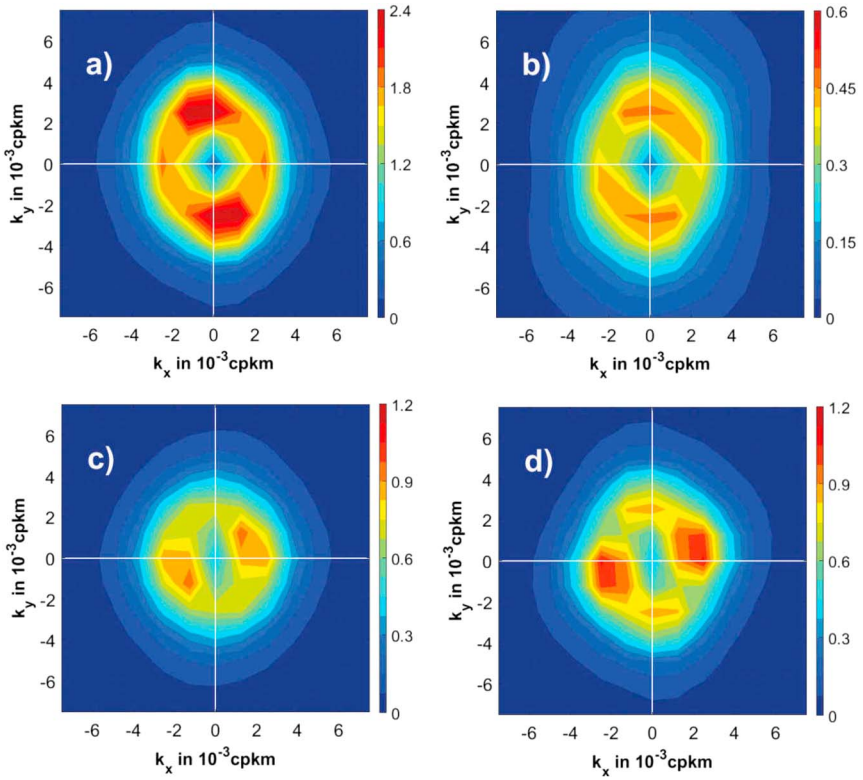

Figure 4. EKE power spectral density distributions as a function of k_x and k_y in the (a, b) upstream and (c, d) downstream when KE is (left) unstable and (right) stable. Unit is in 10^{-9} m^2/s^2.

southern recirculation gyre. In both states, ECCO2 successfully captures the spatial patterns of the observed background circulation and regional EKE, indicating again that ECCO2 is reliable for the investigation of the decadal variability of EKE in the KE region. In the following discussion, we assess the eddy characteristics in the decadal evolution based on the ECCO2 output.

To clarify the spatial characteristics of eddies in the vicinity of the KE jet, we plot in Figure 4 the EKE power spectral density

$$E(k_x, k_y, t) = \frac{1}{2}\left(\hat{u}'\hat{u}'* + \hat{v}'\hat{v}'*\right), \tag{2}$$

as a function of zonal and meridional wave number k_x and k_y for the unstable and stable states, respectively. In equation (2), caret and star indicate discrete Fourier transform and the corresponding complex conjugate, respectively. For these calculations, the velocity anomaly data were preprocessed as follows (Qiu et al., 2008): The velocity anomaly data were partitioned into eight overlapping boxes with 32 × 32 grid points (8° × 8°), centered at 35°N, and every 2° longitude from 146°E to 160°E (gray boxes in Figure 2a). For each box and each time step, the velocity anomaly fields are first detrended by fitting a bilinear plane via least squares. A Hanning window is then applied to the detrended data. The averages over the first (last) three boxes from west are used to evaluate the EKE spectra in the upstream (downstream) KE.

In the upstream KE (Figures 4a and 4b), the eddy signals have a higher-energy level at large k_y than large k_x ranges, implying that the mesoscale eddies are more zonally than meridionally elongated. Compared to the upstream, high-energy level is found to appear at larger k_x range in the downstream, which indicates that eddies in this region are more meridionally elongated (Figures 4c and 4d). This is further confirmed by calculating the eddy elongation parameter

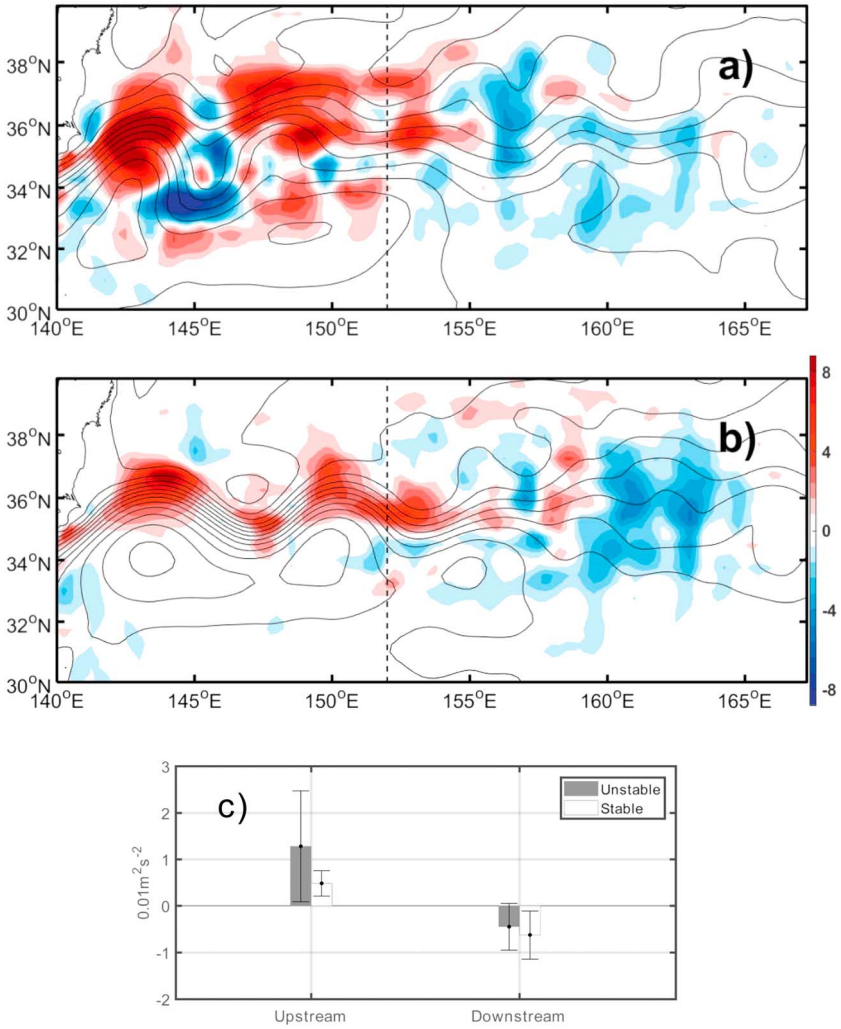

Figure 5. Spatial distribution of M (colored shading; 0.01 m^2/s^2) when KE is (a) unstable and (b) stable. Contours are state-mean SSH isolines. (c) Area-averaged value of M (upstream: 142°E–148°E, 32.5°N–36.5°N; downstream: 153°E–164°E, 33.5°N–38.5°N). Error bars indicate the temporal standard deviation. The black dash lines in (a) and (b) indicate 152°E.

$$M = \frac{1}{2}\left(u'^2 - v'^2\right), \tag{3}$$

where u' and v' are velocity anomalies given in equation (1) (Waterman & Hoskins, 2013). M is an element of eddy Reynolds stresses, which is related to the energy transfer between eddy and mean flow. When M is positive (negative), eddies are zonally (meridionally) elongated and energy is confined to large k_y (k_x) than at large k_x(k_y). Figures 5a and 5b show the spatial distributions of M for the unstable and stable states, respectively. During the unstable period, M in the upstream (142°E–148°E, 32.5°N–36.5°N) is characterized by large positive values around the two crests of the meandering KE. In between them, there is a negative spot on the jet axis in the vicinity of the meander, a region where the EKE level is highest (Figure 3c). Distinct from the unstable state, the M values are always positive in the upstream when KE is stable. Compared to the upstream, M tends to be negative in the downstream (153°E–164°E, 33.5°N–38.5°N) east of 155°E for both states. The area-integrated value of M in the upstream (downstream) is positive (negative), consistent with the spectral analysis (Figure 5c). In addition, it can also be inferred from Figure 5 that eddies tend to be elongated along (against) the mean jet axis in the upstream (downstream). According to Waterman and Hoskins (2013), this implies that eddies draw energy from the mean flow in the upstream and give energy back to mean flow in the downstream. In the following section, we will examine this in detail based on an eddy energy budget analysis.

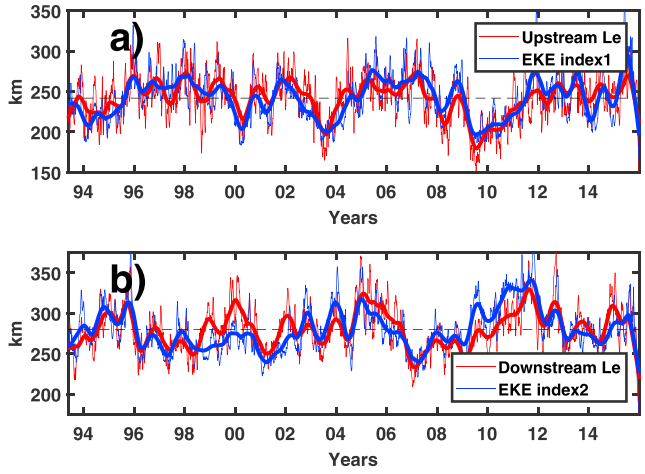

Figure 6. Time series of eddy length scale L_e and EKE index in (a) upstream and (b) downstream KE.

Besides the spatial symmetry, an energy-weighted length scale is also examined, which is defined by

$$L_e(t) = 2\pi \sum_{k_x,k_y} E(k_x,k_y,t)\Delta k^2 / \sum_{k_x,k_y} \left[K \times E(k_x,k_y,t)\right]\Delta k^2, \quad (4)$$

where $K = \sqrt{k_x^2 + k_y^2}$ is the total wave number. The time series in Figure 6 illustrate that L_e experiences very similar decadal modulations as the eddy activity during the past 23 years: a stronger eddy activity corresponds to a larger L_e, whereas a lower EKE level tends to be accompanied by a smaller L_e. The correlations between L_e and regional EKE level are 0.7 and 0.6 in the upstream and downstream regions, respectively. The mean value of L_e in the KE region is about 250 km, close to previous studies using altimetry observations (Wang et al., 2015).

4. Eddy Energetics

In the previous section, it is noted that the decadal evolution of the eddy activity in the upstream and downstream exhibits an out-of-phase relationship. To understand the dynamics controlling the eddy activity more effectively, we consider the eddy energetics in the upstream and downstream KE regions separately in this section.

4.1. Upstream KE

A necessary step to investigate the mechanism that controls the low-frequency variability of eddy activity in the upstream KE system is to understand the associated dynamical processes. To describe these processes, we first examine the prominent unstable and stable events based on EKE index1. When the EKE index1 remains larger (smaller) than +1 (−1) for more than 30 days, we define it as an occurrence of an unstable (a stable) event. According to this definition, 10 unstable (6 stable) events are identified. Their combined time span is 660 days (880 days) and accounts for 51% (70%) of the total samples when the EKE index1 is larger than +1 (smaller than −1). Data information of these events is given in Table 1. In addition, we have changed the criteria (30 days) successively from 24 to 36 days and found that the main conclusions remain similar.

Table 1
Information of the Unstable and Events Based on EKE Index1 in the Upstream KE Region

No.	Start data	End data	Shedding data
a) Unstable events			
1	6 May 1996	25 Aug 1996	21 May 1996
2	3 Apr 1999	15 May 1999	18 Apr 1999
3	29 Mar 2005	15 Jul 2005	25 Apr 2005
4	24 Mar 2006	26 Apr 2006	14 Apr 2006
5	04 Mar 2007	21 May 2007	31 Mar 2007
6	24 Sep 2007	23 Nov 2007	15 Oct 2007
7	29 Jul 2008	17 Nov 2008	24 Sep 2008
8	5 Jul 2011	27 Sep 2011	26 Jul 2011
9	9 Jun 2013	27 Jul 2013	21 Jul 2013
10	9 May 2015	23 Jun 2015	2 Jun 2015
No.	Start data	End data	
b) Stable events			
1	24 Dec 1993	13 Feb 1994	
2	31 Dec 1994	11 Feb 1995	
3	28 Nov 2002	15 Apr 2003	
4	9 May 2003	7 Jan 2004	
5	20 Mar 2009	21 Jul 2009	
6	27 Jan 2011	20 Jul 2011	

By exploring the evolution of SSH during the 10 unstable events, it is found that all events are associated with similar eddy shedding processes in the first quasi-stationary meander. Figure 7 shows the composite SSH maps for the 10 unstable events with time indicating the days relative to the date of eddy detachment. Ninety days before the eddy shedding, the KE is characterized by the presence of two quasi-stationary meanders with their ridges located at 143°E and 149°E, respectively. Subsequently, the meander in the upstream KE begins to form in the trough around 146°E and expands southeastward (Figure 7a). With the strengthening of the meander, both the KE and the southern recirculation are intensified. A prominent cyclonic eddy is developed thereafter on the northern side of the jet 45 days before the eddy shedding (Figure 7b). After its generation, the cyclonic eddy quickly strengthens and continues to intrude southward accompanying the development of the meander (Figure 7c). Finally, the neck of the meander is pinched off, resulting in the detachment of the cyclonic eddy from KE (Figure 7d). The pinched-off eddy moves westward and is found to be dissipated or reabsorbed by the KE east of the Japan coast (Figure 7e). This scenario is very similar to those derived from satellite observations (not shown) and those described in previous studies (Nakano et al., 2013; Qiu et al., 2007; Sasaki & Minobe, 2015).

To clarify the dominant eddy energy sources and sinks during this process, we examine the energy budget based on the equation (Figure 8):

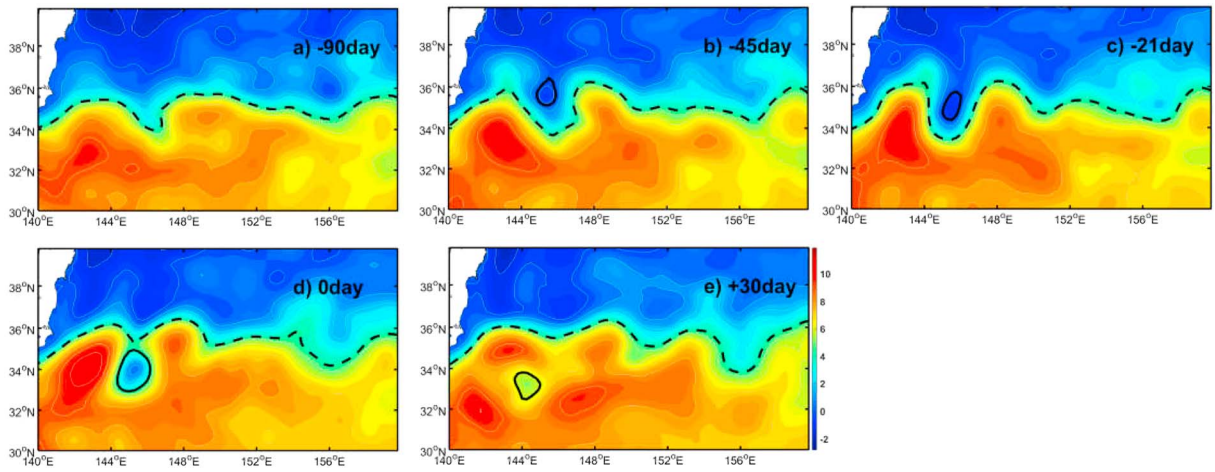

Figure 7. Composite SSH (colored shading; 0.1 m) based on 10 selected unstable events. The time in top-right corner of each panel denotes days before (negative value) or after (positive value) the detachment. The black dash lines denote the 0.42-m SSH contours, which indicate the KE jet. The black solid lines are the outermost enclosed contours in that region, which represent the cyclonic eddy.

$$\rho_0\frac{\partial}{\partial t}\mathrm{EKE}_1=\rho_0\frac{\partial}{\partial t}\frac{\widetilde{u}^2+\widetilde{v}^2}{2}= \underbrace{-\rho_0(\widetilde{u}\widetilde{\mathbf{v}}\cdot\nabla\overline{u}+\widetilde{v}\widetilde{\mathbf{v}}\cdot\nabla\overline{v})}_{\mathrm{BT}}\ \underbrace{-\widetilde{\rho}\widetilde{w}g}_{\mathrm{BF}}\ \underbrace{-\nabla\cdot\left[\frac{1}{2}\rho_0\mathbf{v}\left(\widetilde{u}^2+\widetilde{v}^2\right)+\widetilde{p}\widetilde{\mathbf{v}}\right]}_{Q}+E_k, \tag{5}$$

where $\mathbf{v}=(u, v, w)$ represents velocity vector, ρ is the density, and p indicates pressure. The symbol ∇ represents the three-dimensional gradient operator, overbar indicates time mean, and tilde indicates anomaly. The detailed derivation of equation (5) is given in Appendix A. In this equation, $-\widetilde{\rho}\widetilde{w}g$, the first term on the right-hand side describes EKE generation by the release of eddy available potential energy (EAPE) through

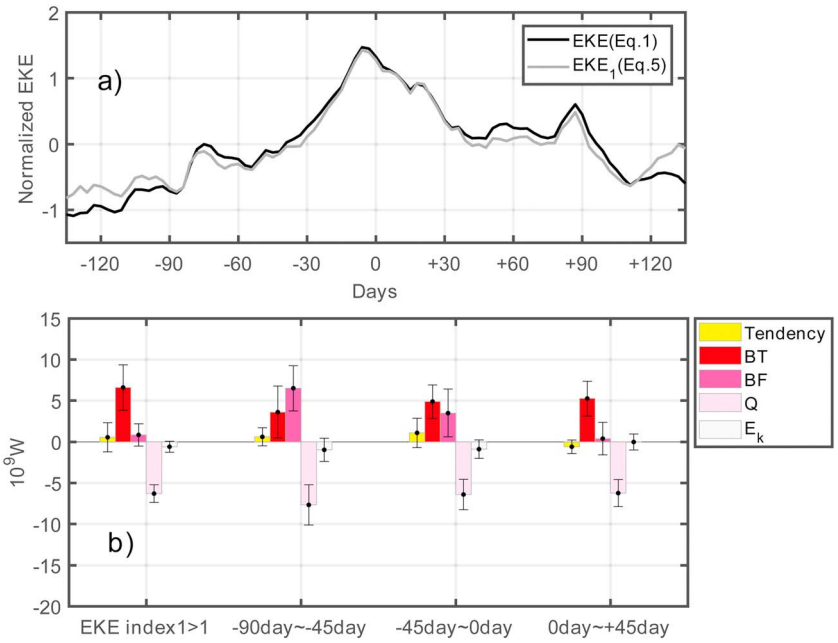

Figure 8. (a) Time series of normalized composite-EKE during 10 unstable events based on equations (1) and (5), respectively. The time denotes days before (negative value) or after (positive value) the detachment. (b) Eddy energy budget in the unstable events integrated over the upstream KE region (142°E–152E, 31°N–39°N) in the upper 1,500 m. Error bars indicate the standard deviation of 10 events.

buoyancy forcing (BF) associated with BC. $-\rho_0(\widetilde{u}\widetilde{\mathbf{v}}\cdot\nabla\overline{u}+\widetilde{v}\widetilde{\mathbf{v}}\cdot\nabla\overline{v})$ denotes the product of eddy momentum flux and gradient of background flow and represents the energy transfer between mean flow and eddies through BT. The Q term denotes the nonlocal process of energy flux divergence through advection and pressure work. The term E_k represents the change rate of EKE due to friction, wind stress, and bottom drag. This term is not explicitly diagnosed, as certain variables are not available in the ECCO2 output. For each case, the period used to calculate the time mean is from 135 days before the eddy shedding to 135 days after the eddy shedding (270 days in total). EKE_1 based on this definition is consistent with EKE defined in equation (1) (Figure 8a). Based on both definitions, the EKE level reaches maximum around the day of eddy detachment. In addition, we have also changed the period successively from 240 to 300 days and found that the results are insensitive to the period selection.

Figure 8b shows the composite energy budget of EKE during the 10 eddy shedding events integrated in the upper 1,500 m layer within the area 142°E–152°E, 31°N–39°N. Changing the depth from 1,000 to 2,000 m does not change the relative importance of the eddy energy terms. To get a better understanding of the dynamics, horizontal distributions of BF and BT are also provided (Figure 9). Before the cyclonic eddy appears (−90 to −45 day), significant energy conversion from EAPE to EKE is found along the KE jet with high values west of 146°E (Figure 9a). In addition to the EAPE releasing, perturbations also draw their energy from the mean flow through BT (Figure 9e), especially near the first crest of the meandering KE jet (142.5°E, 35°N). Quantitatively, BF and BT contribute about 65% and 35% of the total EKE source, respectively. After the eddy is generated (−45 to 0 day), it grows quickly accompanying the development of meander. In this stage, BF is characterized by positive (negative) values around the western (eastern) part of the meander (Figure 9b). This feature is associated with the negative (positive) vertical velocity anomaly western (eastern) of the meander trough (Bishop, 2013). Compared to that, significant positive BT emerges in the vicinity of the well-developed meander, suggesting a potential role of meander in elevating the barotropic energy exchange (Figure 9f). By integrating over the upstream KE, it is shown that contributions from BT and BF are comparable during this period (Figure 8b). Once the cyclonic eddy is pinched off (0 to +45 days), it propagates westward and gradually moves away from the KE jet. During this period, the barotropic energy conversion prevails, while the baroclinic energy conversion experiences a sharp decrease. Large positive BT is found around the detachment, position of eddy (146°E, 34°N; Figure 9g), which may be associated with the strong horizontal shear of the eddy when it is just pinched off. Averaged over the periods when EKE index1 is larger than +1, the patterns of both BF and BC bear resemblance to those for −45 to 0 day and BT is the main EKE source (90%), while BF plays a secondary role (10%). During the eddy shedding process, the divergent term Q always acts as an energy sink, transporting eddy energy out of the domain. Moreover, Q is found to reach its minimum, just before the eddy detachment when the meander is fully developed, in accordance with the theory by Abernathey and Cessi (2014) that meanders are able to concentrate eddy activity. In addition, the value of residual term E_k is always negative and much smaller than the eddy energy sources and sinks, a result obtained by Yang et al. (2017) as well.

Our above analysis indicates that the unstable process is mainly triggered by the generation of a cyclonic eddy associated with BC. To further confirm this, we analyze the stability properties of the KE based on the multilayer quasi-geostrophic model (Smith, 2007; Appendix B). By numerically solving the eigenvalue problem, for linear instability of the KE during −90 to −45 day, we obtain the growth rate of unstable waves as a function of two-dimensional wave numbers. For this calculation, the mean state is chosen based on the averaged velocity, salinity, and temperature in the vicinity of KE between 142°E and the trough of meander (e.g. 145°E in Figure 9a) for each case. It is found that the most unstable wave occurs at 154 ± 38 km with the growth rate 0.02 ± 0.007 day^{-1}, which is comparable to the size of the cyclonic eddy during its generation stage (Figure 7b). Note that this length scale is smaller than the energy-containing wavelength in the unstable state (L_e ~250 km), which points to the possibility of an inverse EKE cascade. This is examined by calculating the spectral kinetic energy flux in the wave number space following Scott and Wang (2005):

$$\Pi_K=\mathbf{v}_{hK}^{<}\cdot\left(\mathbf{v}_{hK}^{<}\cdot\nabla\mathbf{v}_{hK}^{>}\right)+\mathbf{v}_{hK}^{<}\cdot\left(\mathbf{v}_{hK}^{>}\cdot\nabla\mathbf{v}_{hK}^{>}\right), \tag{6}$$

where $\mathbf{v}_h=(u,v)$ represents the horizontal velocity vector and $^{<}_{K}(^{>}_{K})$ denotes the low-pass (high-pass) filter with respect to the horizontal total wave number K. A positive (negative) value of Π_K indicates that the kinetic

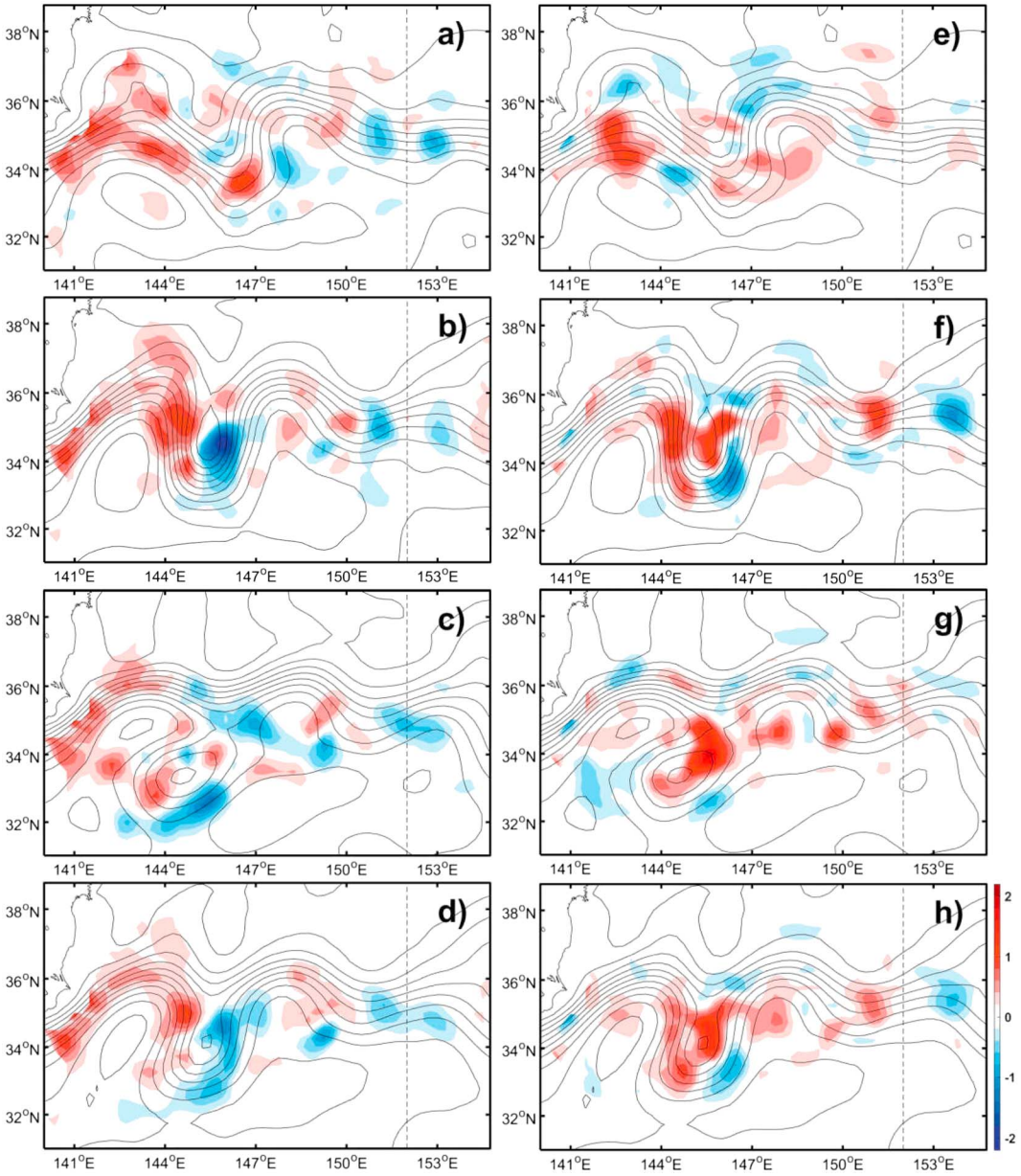

Figure 9. Composite horizontal distribution of (left) BF and (right) BT (colored shading; 10^8 W) integrated over upper 1,500 m in the 10 unstable events during (a) −90 to −45 day, (b) −45 to 0 day, (c) 0 to +45 days, and (d) EKE index1 > +1. Contours are coinstantaneous mean SSH isolines. The black dash lines indicate 152°E.

energy is transferred from a larger (smaller) spatial scale to a smaller (larger) one, indicative of a forward (inverse) cascade. The methods used to preprocess the horizontal velocity are the same as calculating $E(k_x, k_y, t)$ in equation (2). Figure 10 shows Π_K during the generation period of the cyclonic eddy (−90 to −45 day; in blue). For comparison, the corresponding spectral kinetic energy density defined by

$$E(K,t) = \sum_{K^2=k_x^2+k_y^2} E\left(k_x, k_y, t\right), \tag{7}$$

is also plotted (in red). It is found that the energy source (the steepest positive slope of Π_K) is located at around 160 km, which is close to the value based on the linear stability analysis (Figure 10). This result supports, the conclusion of energy budget that baroclinic pathway is the main EKE source during this

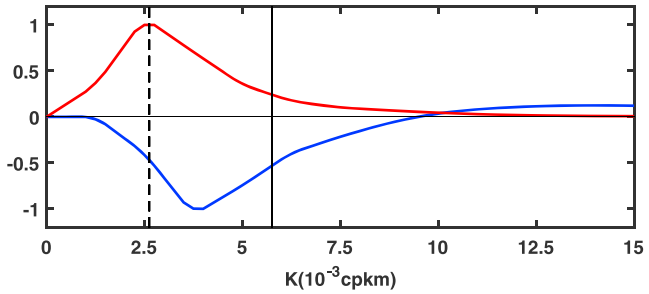

Figure 10. Spectral kinetic energy flux Π (blue) and spectral kinetic energy density (red) in the upstream KE during -90 to -45 days. All the curves are normalized by their maximum of absolute value. The solid vertical line denotes the scales of energy source, and dashed line indicates energy sink.

period. Meanwhile, the peak of E (K, t) falls on the left shoulder of the inverse cascade, and is identifiable as the energy sink (the steepest negative, slope of Π_K) scale. This consistency suggests that the evolution of EKE during this period can be explained in terms of BC and inverse cascade., During the following, two stages, the distributions of Π_K are characterized, by energy sources with larger length scales, which may imply the potential role of BT in regulating the spatial kinetic energy flux (not shown).

Besides the unstable events, evolution of the SSH and eddy energetics in the stable events are assessed as well. Among all of the six stable events (Table 1b), neither large meander nor eddy shedding is detected. Eddy energy budget during the stable state (EKE index1 < -1) and horizontal distribution of energy sources are shown in Figure 11. In the calculation, the mean flow is defined as the time mean of 270 days with respect to the middle time point for each event. This is also consistent with the definition in equation (1) (not shown). During the stable state, both BF and BT are confined to the vicinity of KE jet (Figures 11b and 11c). Positive BF is found to emerge along the whole upstream KE, while BT is characterized by three positive lobes located at 145°E, 147°E, and 149°E, respectively. Integrating over the upstream KE, the baroclinic pathway constitutes the major energy source of EKE and accounts for 70% of the total energy source. The generated eddy energy is mainly transported out of the domain by Q (Figure 11a). Moreover, the stability properties of the KE and kinetic energy spectral flux during the stable state are also estimated. The most unstable wave occurs at 166 ± 20 km (growth rate 0.025 ± 0.01 day^{-1}), which resembles the length scale of energy source. The maximum, of spectral kinetic energy density is found to be consistent with the scale of energy sink (about 2.5×10^{-3} cp/km, not shown). These indicate that the eddy field in the upstream KE during the stable state is a result of BC and inverse cascade.

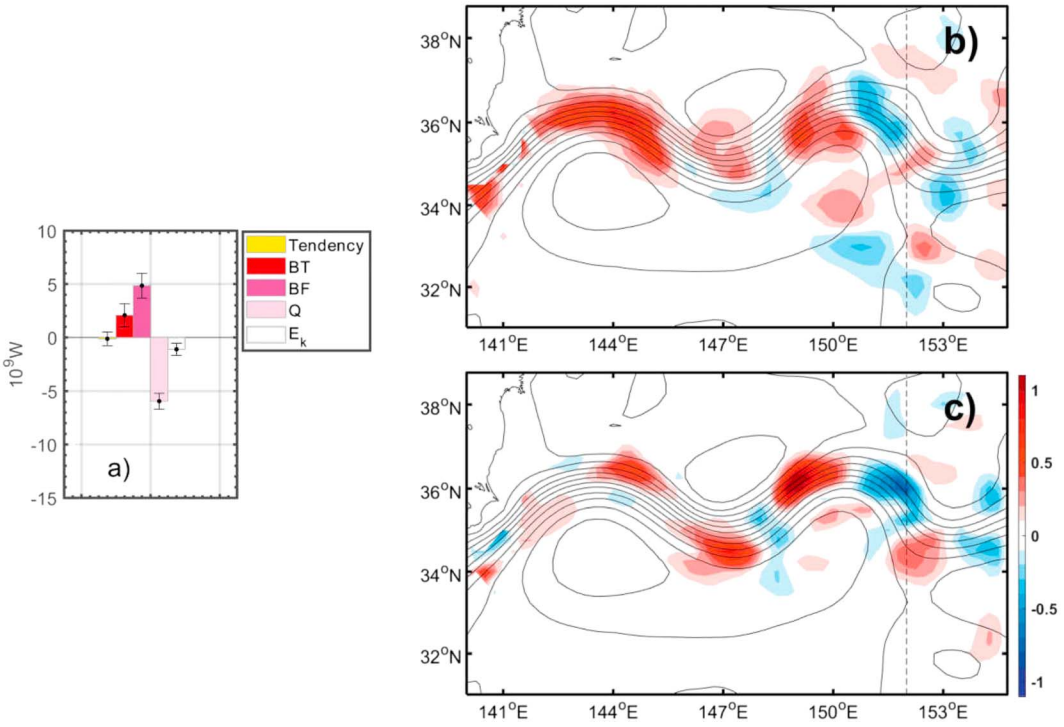

Figure 11. (a) Eddy energy budget in the stable events integrated over the upstream KE region (142°E–152E, 31°N–39°N) in the upper 1,500 m. Error bars indicate the standard deviation of six events. Composite horizontal distribution of (b) BF and (c) BT (colored shading; 10^8 W) integrated over upper 1,500 m in the stable events. The black dash lines in (b) and (c) indicate 152°E.

Table 2
Information of the Unstable and Events Based on EKE Index2 in the Downstream KE Region

No.	Start data	End data	No.	Start data	End data
a) Unstable events					
1	9 Aug 1994	13 Nov 1994	7	22 Apr 2009	26 Aug 2009
2	18 Oct 1995	29 Nov 1995	8	30 Mar 2010	2 May 2010
3	13 Feb 2002	6 Apr 2002	9	2 Sep 2010	10 Nov 2010
4	2 Sep 2002	28 Nov 2002	10	27 Jan 2011	26 Feb 2011
5	29 Dec 2003	6 Feb 2004	11	29 Jul 2011	11 Dec 2011
6	27 Sep 2004	28 Jan 2005	12	15 Sep 2012	18 Oct 2012
b) Stable events					
1	27 Feb 1996	31 Mar 1996	7	15 May 2007	17 Jul 2007
2	11 Dec 1996	29 Mar 1997	8	14 Dec 2008	24 Feb 2009
3	3 Mar 1998	5 Apr 1998	9	19 Jan 2013	17 Mar 2013
4	8 Sep 1998	23 Oct 1998			
5	4 Jan 2001	24 Feb 2001			
6	26 Sep 2006	18 Apr 2007			

4.2. Downstream KE

Similar to the upstream, 12 unstable events and 9 stable events in the downstream KE are identified (Table 2) based on the EKE index2. The combined time span for the unstable (stable) events is 1,035 days (780 days) and accounts for 77% (65%) of the total samples when EKE index2 is larger (smaller) than +1 (−1). Compared to those in the upstream region, the unstable events in the downstream KE are much more complex. Shedding and absorption of both cyclonic and anticyclonic eddies can be detected in one event. Here we take the event between 8 August and 12 November 1994, as an example. On 7 September, an anticyclonic eddy was pinched off from the KE jet around 154°E, 37°N (Figure 12a) and was then reabsorbed by KE 9 days later (Figure 12b). Meanwhile, two cyclonic eddies were generated respectively at 155°E, 34.5°N and 162°E, 34°N and shed from KE (Figure 12c). On 6 November, an anticyclonic eddy was formed at 154°E, 38°N (Figure 12d). Different from the high-EKE periods, the downstream KE in the low-EKE stage is relatively stable with few eddy shedding cases (not shown).

Based on equation (5), the eddy energy budget for the downstream KE is estimated (Figure 13). In the calculation, the mean flow is defined as the time mean of 270 days with respect to the middle time point for each event. In both dynamical states, the divergent term Q is the main energy source and 60% of which is dissipated through E_k. Further exploration reveals that Q is dominated by advection from the west, indicating that the major portion of the energy fed into the downstream EKE is supplied by the upstream inflow. This is in accordance with the meridionally elongated structure of eddies in this region. Compared to the stable state, Figure 13 shows that Q is significantly larger when the downstream KE is unstable, which makes it a major factor in determining the decadal EKE variability. This seems inconsistent with the above conclusions that the correlation between the EKE levels in the upstream and downstream is negative and that the Q term is larger during the unstable period of upstream (Figures 8b and 11). To explain this inconsistency, we decompose Q of the upstream KE into horizontal and vertical components (not shown). It is found that the horizontal component of Q is more dominant when the upstream KE is stable, in

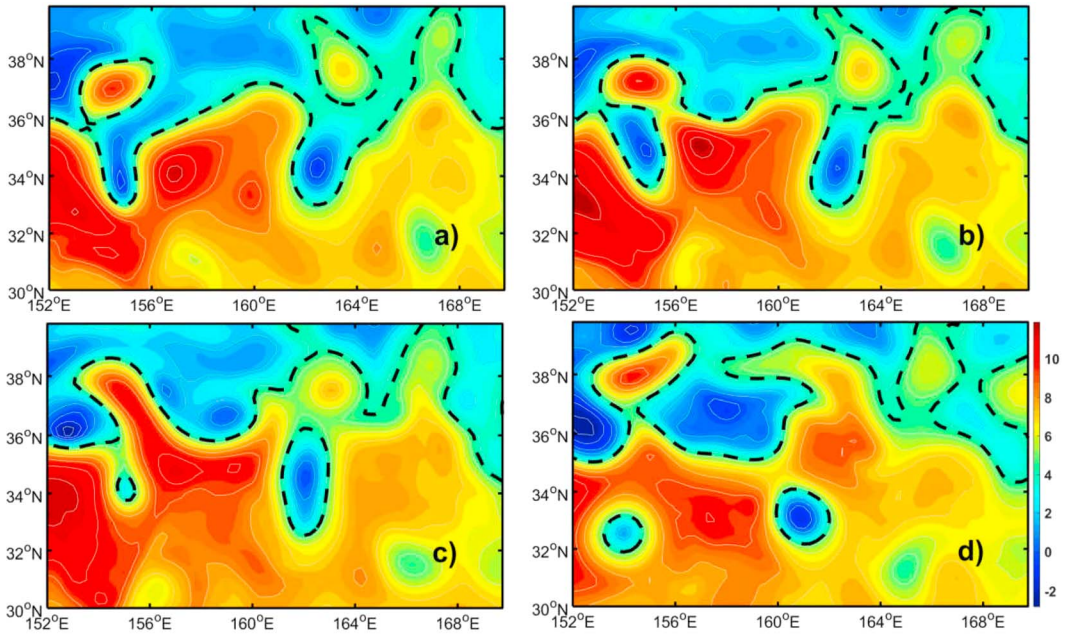

Figure 12. Snapshot of SSH field (colored shading; 0.1 m) on (a) 7 September 1994, (b) 16 September 1994, (c) 28 September 1994, and (d) 6 November 1994. The black dash lines denote the 0.42-m SSH contours.

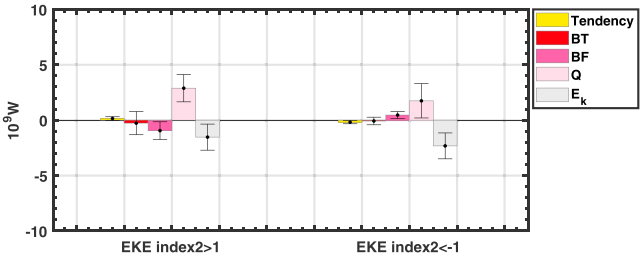

Figure 13. Eddy energy budget integrated over the downstream KE region (153°E–165°E, 31°N–39°N) in the upper 1,500 m. Error bars indicate the standard deviation of events.

accordance with analysis in the downstream. It is noted that BF plays different roles during the two states. During the unstable state, BF is largely negative, implying that energy is fluxed back from EKE to EAPE. This result is in accordance with previous estimations (Chen et al., 2014). However, the negative values are overcompensated by the large positive ones at 159°E in the stable state, which may be induced by the flow-topography interaction around the Skatsky Rise (Qiu & Chen, 2011; Sasaki & Minobe, 2015) as the jet is stronger in this state (not shown). Overall, the energy budget illustrates that the downstream KE region is a graveyard for the eddy energy and the decadal EKE evolution is mainly regulated by the upstream KE.

5. Summary and Discussion

Based on the ECCO2 state estimate from 1993 to 2015, the decadal variability of eddy characteristics and their dynamical mechanisms during the stable and unstable states of the KE are explored in this study. Based on the EOF analysis, it is found that the decadal evolution of eddy kinetic energy in the KE region is characterized by a delayed negative correlation between the upstream and downstream when the upstream leads by 300 days and the EKE variability in the broad KE region is dominated by its upstream component. In addition to the out-of-phase change in eddy activity levels, the eddy characteristics and energetics in the upstream KE are also different from those in the downstream. In the upstream KE, eddies are zonally stretched on average, whereas they tend to be stretched in the meridional direction in the downstream region. Consistently, eddies are found to draw energy from the mean flow in the upstream and give energy back to the mean flow in the downstream, in accordance with the previous study (Waterman & Hoskins, 2013). Unstable events in the upstream KE are characterized by strong eddy-shedding processes. During these events, cyclonic eddies are found to be formed in the first quasi-stationary meander and finally pinched off from the KE jet. The energy budget analysis illustrates that the eddy shedding processes are triggered by the generation of cyclonic eddies due to BC, while barotropic energy transfer becomes the main energy source for eddy growth when the meander is fully developed. Accompanied by the eddy generation, significant inverse energy cascade is detected. In comparison, evolution of eddy activity can be explained in terms of BC and inverse energy cascade when the upstream KE is stable. Different from its upstream, counterpart, the downstream KE acts as a graveyard for eddy energy. The decadal EKE variability in this region is mainly regulated by the upstream condition through lateral advection.

This study explores in great depth the dynamical processes shared by all unstable events in the upstream KE and analyzes the evolution of eddy energetics during these processes. A better understanding of these processes in the KE region will likely be beneficial to the understanding of low-frequency variability in other strong oceanic current regions in the global ocean. In addition, it should be also noted that more studies are required to clarify the roles played by friction, wind work, and bottom drag in the residual term E_k. Processes associated with the flow-topography and eddy-topography interactions, which may affect the eddy energy (Qiu & Chen, 2005), are not fully analyzed in the present study. Furthermore, ocean mesoscale eddy-atmosphere interactions through surface turbulent heat flux exchange in the KE region have been found to be important in maintaining the eddy potential energy budget (e.g., Ma et al., 2016); ocean current feedback on wind stresses is also shown to have an important impact on EKE through wind work (e.g., Renault et al., 2016, 2017). How ocean mesoscale eddy-atmosphere interactions can modulate the dynamical state of KE should be investigated in future studies using high-resolution observations and coupled model simulations.

Appendix A: Eddy Energy Equation

Considering the equations with hydrostatic and Boussinesq approximations,

$$\frac{\partial u}{\partial t}+\nabla\cdot(u\mathbf{v})-fv=-\frac{1}{\rho_0}\frac{\partial p}{\partial x}+F_u, \tag{A1}$$

$$\frac{\partial v}{\partial t}+\nabla\cdot(v\mathbf{v})+fu=-\frac{1}{\rho_0}\frac{\partial p}{\partial y}+F_v, \tag{A2}$$

$$\nabla\cdot\mathbf{v} = 0, \quad \text{and} \tag{A3}$$

$$\frac{\partial p}{\partial z} = -\rho g, \tag{A4}$$

where $\mathbf{v} = (u, v, w)$ is the three-dimensional velocity vector, term p is the hydrostatic pressure, and F is the external forcing and dissipation. The symbol ∇ represents the three-dimensional Laplacian operator. The variables are decomposed into their time-mean and anomaly state as $A = \overline{A} + \widetilde{A}$ (overbar is time mean and wave indicates anomaly). Taking the time-varying component of equation (A4) and multiplying by $\widetilde{w}$ to get

$$\frac{\partial \widetilde{p}}{\partial z}\widetilde{w} = -\widetilde{\rho}\widetilde{w}g. \tag{A5}$$

Using equation (A3), we have

$$\frac{\partial(\widetilde{p}\widetilde{w})}{\partial z} + \widetilde{p}\left(\frac{\partial \widetilde{u}}{\partial x} + \frac{\partial \widetilde{v}}{\partial x}\right) = -\widetilde{\rho}\widetilde{w}g. \tag{A6}$$

Multiplying the time-varying component of equations (A1) and (A2) by $\widetilde{u}$ and $\widetilde{v}$, respectively, summing them together, and substituting it into equation (A6), we obtain equation (5).

Appendix B: Linear Stability Analysis

Considering the linear quasi-geostrophic equation,

$$\frac{\partial q}{\partial t} + \mathbf{U}\cdot\nabla q + \mathbf{u}\cdot\nabla Q = 0, \quad -H < z < 0, \tag{B1a}$$

$$\frac{\partial}{\partial t}\left(\frac{\partial \psi}{\partial z}\right) + \mathbf{U}\cdot\nabla\frac{\partial \psi}{\partial z} + \mathbf{u}\cdot\nabla\left(\frac{\partial \Psi}{\partial z}\right) = 0, \quad z = -H, 0, \tag{B1b}$$

where $\psi(x, y, z, t)$ represents the eddy horizontal stream function, $q = \nabla^2\psi + \Gamma\psi$ is the eddy quasi-geostrophic potential vorticity, and $\mathbf{u} = \left(-\frac{\partial \psi}{\partial y}, \frac{\partial \psi}{\partial x}\right)$ is the eddy velocity field. $\Psi(z)$, $Q(z)$, and $\mathbf{U}(z)$ are the mean of ψ, q, and $\mathbf{u}$, respectively. The symbol ∇ represents the Laplacian operator, and Γ is defined as $\Gamma A = \frac{d}{dz}\left(\frac{f^2}{N^2}\frac{dA}{dz}\right)$.

Let $\psi(x, y, z, t) = \text{Re}\{\phi(z)e^{i(kx + ly - wt)}\}$, and we obtain

$$(\mathbf{K}\cdot\mathbf{U} - \omega)(\Gamma - K^2)\phi = \left(\frac{\partial Q}{\partial x}l - \frac{\partial Q}{\partial y}k\right)\phi, \quad -H < z < 0, \tag{B2a}$$

$$(\mathbf{K}\cdot\mathbf{U} - \omega)\frac{\partial \phi}{\partial z} = \left(k\frac{\partial U}{\partial z} + l\frac{\partial V}{\partial z}\right), \quad z = -H, 0. \tag{B2b}$$

Here $\mathbf{K} = (k, l)$ and $K = (k^2 + l^2)^{1/2}$. Equations (B2a) and (B2b) form an eigenvalue problem for the normal modes ϕ and the frequency ω exponentially. For more information about this mathematic model, readers are referred to Smith (2007).

Acknowledgments
This research is supported by National key research and development program of China (2016YFC1402606), National Natural Science Foundation of China (41490640, 41521091, U1606402, and 41527901), and Aoshan Program supported by Pilot National Laboratory for Marine Science and Technology (Qingdao) (2015ASKJ01, 2017ASKJ01, and 2017ASTCPES05). H. Y. is partially supported by the Chinese Scholarship Council. The ECCO2 and AVISO products used this study can be obtained through the URL http://apdrc.soest.hawaii.edu/data/ and http://www.aviso.oceanobs.com/, respectively. The authors wish to thank Ru Chen for providing the program to calculate the oceanic density field.

References

Abernathey, R., & Cessi, P. (2014). Topographic enhancement of eddy efficiency in baroclinic equilibration. *Journal of Physical Oceanography*, *44*(8), 2107–2126. https://doi.org/10.1175/JPO-D-14-0014.1

Adcroft, A., Campin, J., Hill, C., & Marshall, J. (2004). Implementation of an atmosphere–ocean general circulation model on the expanded spherical cube. *Monthly Weather Review*, *132*(12), 2845–2863. https://doi.org/10.1175/MWR2823.1

Berloff, P., Hogg, A., & Dewar, W. (2007). The turbulent oscillator: A mechanism of low-frequency variability of the wind-driven ocean gyres. *Journal of Physical Oceanography*, *37*(9), 2363–2386. https://doi.org/10.1175/JPO3118.1

Bishop, S. (2013). Divergent eddy heat fluxes in the Kuroshio Extension at 144°–148°E. Part II: Spatiotemporal variability. *Journal of Physical Oceanography*, *43*(11), 2416–2431. https://doi.org/10.1175/JPO-D-13-061.1

Ceballos, L., Di Lorenzo, E., Hoyos, C., Schneider, N., & Taguchi, B. (2009). North Pacific gyre oscillation synchronizes climate fluctuations in the eastern and western boundary systems. *Journal of Climate*, *22*(19), 5163–5174. https://doi.org/10.1175/2009JCLI2848.1

Chen, R., Flierl, G., & Wunsch, C. (2014). A description of local and nonlocal eddy–mean flow interaction in a global eddy-permitting state estimate. *Journal of Physical Oceanography*, *44*(9), 2336–2352. https://doi.org/10.1175/JPO-D-14-0009.1

Deser, C., Alexander, M., & Timlin, M. (1999). Evidence for a wind-driven intensification of the Kuroshio Current Extension from the 1970s to the 1980s. *Journal of Climate*, *12*(6), 1697–1706. https://doi.org/10.1175/1520-0442(1999)012<1697:EFAWDI>2.0.CO;2
Dijkstra, H., & Ghil, M. (2005). Low-frequency variability of the large scale ocean circulation: A dynamical approach. *Reviews of Geophysics*, *43*, RG3002. https://doi.org/10.1029/2002RG000122
Ducet, N., Le Traon, P., & Reverdin, G. (2000). Global high resolution mapping of ocean circulation from TOPEX/Poseidon and ERS-1 and -2. *Journal of Geophysical Research*, *105*(C8), 19,477–19,498. https://doi.org/10.1029/2000JC900063
Ferrari, R., & Wunsch, C. (2009). Ocean circulation kinetic energy: Reservoirs, sources, and sinks. *Annual Review of Fluid Mechanics*, *41*(1), 253–282. https://doi.org/10.1146/annurev.fluid.40.111406.102139
Gill, A., Green, J., & Simmons, A. (1974). Energy partition in the large-scale ocean circulation and the production of mid-ocean eddies. *Deep Sea Research and Oceanographic Abstracts*, *21*(7), 499–528. https://doi.org/10.1016/0011-7471(74)90010-2
Hogg, A., Killworth, P., Blundell, J., & Dewar, W. (2005). Mechanisms of decadal variability of the wind-driven ocean circulation. *Journal of Physical Oceanography*, *35*(4), 512–531. https://doi.org/10.1175/JPO2687.1
Itoh, S., & Yasuda, I. (2010). Characteristics of mesoscale eddies in the Kuroshio–Oyashio Extension region detected from the distribution of the sea surface height anomaly. *Journal of Physical Oceanography*, *40*(5), 1018–1034. https://doi.org/10.1175/2009JPO4265.1
Jia, F., Wu, L., Lan, J., & Qiu, B. (2011). Interannual modulation of eddy kinetic energy in the southeast Indian Ocean by southern annular mode. *Journal of Geophysical Research*, *116*, C02029. https://doi.org/10.1029/2010JC006699
Jiang, S., Jin, F., & Ghil, M. (1995). Multiple equilibria and a periodic solutions in a wind-driven double gyre, shallow water model. *Journal of Physical Oceanography*, *25*(5), 764–786. https://doi.org/10.1175/1520-0485(1995)025<0764:MEPAAS>2.0.CO;2
Joyce, T., Yasuda, I., Hiroe, Y., Komatsu, K., Kawasaki, K., & Bahr, F. (2001). Mixing in the meandering Kuroshio Extension and the formation of North Pacific Intermediate Water. *Journal of Geophysical Research*, *106*(C3), 4397–4404. https://doi.org/10.1029/2000JC000232
Kelly, K., Small, R., Samelson, R., Qiu, B., Joyce, T., Kwon, Y., & Cronin, M. (2010). Western boundary currents and frontal air–sea interaction: Gulf Stream and Kuroshio Extension. *Journal of Climate*, *23*(21), 5644–5667. https://doi.org/10.1175/2010JCLI3346.1
Kida, S., Mitsudera, H., Aoki, S., Guo, X., Ito, S., Kobashi, F., et al. (2015). Oceanic fronts and jets around Japan: A review. *Journal of Oceanography*, *71*(5), 469–497. https://doi.org/10.1007/s10872-015-0283-7
Kwon, Y., Alexander, M., Bond, N., Frankignoul, C., Nakamura, H., Qiu, B., et al. (2010). Role of the Gulf Stream and Kuroshio–Oyashio systems in large-scale atmosphere–ocean interactions: A review. *Journal of Climate*, *23*, 3249–3281.
Large, W., McWilliams, J., & Doney, S. (1994). Oceanic vertical mixing: A review and a model with a nonlocal boundary layer parameterization. *Reviews of Geophysics*, *32*(4), 363–403. https://doi.org/10.1029/94RG01872
Le Traon, P., & Dibarboure, G. (1999). Mesoscale mapping capabilities of multiple-satellite altimeter missions. *Journal of Atmospheric and Oceanic Technology*, *16*, 1208–1223.
Ma, X., Jing, Z., Chang, P., Liu, X., Montuoro, R., Small, R., et al. (2016). Western boundary currents regulated by interaction between ocean eddies and the atmosphere. *Nature*, *535*(7613), 533–537. https://doi.org/10.1038/nature18640
Marshall, J., Adcroft, A., Hill, C., Perelman, L., & Heisey, C. (1997). A finite-volume, incompressible Navier Stokes model for studies of the ocean on parallel computers. *Journal of Geophysical Research*, *102*(C3), 5753–5766. https://doi.org/10.1029/96JC02775
McCalpin, J., & Haidvogel, D. (1996). Phenomenology of the low-frequency variability in a reduced gravity quasi-geostrophic double-gyre model. *Journal of Physical Oceanography*, *26*(5), 739–752. https://doi.org/10.1175/1520-0485(1996)026<0739:POTLFV>2.0.CO;2
Menemenlis, D., Hill, C., Adcrocft, A., Campin, J., Cheng, B., Ciotti, B., et al. (2005). NASA supercomputer improves prospects for ocean climate research. *Eos, Transactions American Geophysical Union*, *86*(9), 89–96. https://doi.org/10.1029/2005EO090002
Miller, A., Cayan, D., & White, W. (1998). A westward intensified decadal change in the North Pacific thermocline and gyre-scale circulation. *Journal of Climate*, *11*(12), 3112–3127. https://doi.org/10.1175/1520-0442(1998)011<3112:AWIDCI>2.0.CO;2
Nakano, H., Tsujino, H., & Sakamoto, K. (2013). Tracer transport in cold-core rings pinched off from the Kuroshio Extension in an eddy-resolving ocean general circulation model. *Journal of Geophysical Research: Oceans*, *118*, 5461–5488. https://doi.org/10.1002/jgrc.20375
North, G., Moeng, F., Bell, T., & Cahalan, R. (1982). Sampling errors in the estimation of empirical orthogonal functions. *Monthly Weather Review*, *110*(7), 699–706. https://doi.org/10.1175/1520-0493(1982)110<0699:SEITEO>2.0.CO;2
Pedlosky, J. (1987). *Geophysical fluid dynamics* (2nd ed., p. 710). New York: Springer. https://doi.org/10.1007/978-1-4612-4650-3
Penduff, T., Barnier, B., Dewar, W., & O'Brien, J. (2004). Dynamical response of the oceanic eddy field to the North Atlantic Oscillation: A model–data comparison. *Journal of Physical Oceanography*, *34*(12), 2615–2629. https://doi.org/10.1175/JPO2618.1
Pierini, S. (2014). Kuroshio Extension bimodality and the North Pacific Oscillation: A case of intrinsic variability paced by external forcing. *Journal of Climate*, *27*(1), 448–454. https://doi.org/10.1175/JCLI-D-13-00306.1
Pierini, S., Dijkstra, H., & Riccio, A. (2009). A nonlinear theory of the Kuroshio Extension bimodality. *Journal of Physical Oceanography*, *39*(9), 2212–2229. https://doi.org/10.1175/2009JPO4181.1
Primeau, F., & Newman, D. (2008). Elongation and contraction of the western boundary current extension in a shallow-water model: A bifurcation analysis. *Journal of Physical Oceanography*, *38*(7), 1469–1485. https://doi.org/10.1175/2007JPO3658.1
Qiu, B. (2003). Kuroshio Extension variability and forcing of the Pacific decadal oscillations: Responses and potential feedback. *Journal of Physical Oceanography*, *33*(12), 2465–2482. https://doi.org/10.1175/2459.1
Qiu, B., & Chen, S. (2005). Variability of the Kuroshio Extension jet, recirculation gyre, and mesoscale eddies on decadal time scales. *Journal of Physical Oceanography*, *35*(11), 2090–2103. https://doi.org/10.1175/JPO2807.1
Qiu, B., & Chen, S. (2010). Eddy-mean flow interaction in the decadally modulating Kuroshio Extension system. *Deep-Sea Research Part II*, *57*(13-14), 1098–1110. https://doi.org/10.1016/j.dsr2.2008.11.036
Qiu, B., & Chen, S. (2011). Effect of decadal Kuroshio Extension jet and eddy variability on the modification of North Pacific Intermediate Water. *Journal of Physical Oceanography*, *41*(3), 503–515. https://doi.org/10.1175/2010JPO4575.1
Qiu, B., Chen, S., & Hacker, P. (2007). Effect of mesoscale eddies on subtropical mode water variability from the Kuroshio Extension System Study (KESS). *Journal of Physical Oceanography*, *37*(4), 982–1000. https://doi.org/10.1175/JPO3097.1
Qiu, B., Chen, S., Schneider, N., & Taguchi, B. (2014). A coupled decadal prediction of the dynamic state of the Kuroshio Extension system. *Journal of Climate*, *27*(4), 1751–1764. https://doi.org/10.1175/JCLI-D-13-00318.1
Qiu, B., Kelly, K., & Joyce, T. (1991). Mean flow and variability in the Kuroshio Extension from Geosat altimetry data. *Journal of Geophysical Research*, *96*(C10), 18,491–18,507. https://doi.org/10.1029/91JC01834
Qiu, B., Schneider, N., & Chen, S. (2007). Coupled decadal variability in the North Pacific: An observationally constrained idealized model. *Journal of Climate*, *20*(14), 3602–3620. https://doi.org/10.1175/JCLI4190.1
Qiu, B., Scott, R., & Chen, S. (2008). Length scales of eddy generation and nonlinear evolution of the seasonally modulated South Pacific Subtropical Countercurrent. *Journal of Physical Oceanography*, *38*(7), 1515–1528. https://doi.org/10.1175/2007JPO3856.1
Renault, L., McWilliams, J., & Masson, S. (2017). Satellite observations of imprint of oceanic current on wind stress by air-sea coupling. *Scientific Reports*, *7*(1), 17747. https://doi.org/10.1038/s41598-017-17939-1

Renault, L., Molemaker, M., McWilliams, J., Shchepetkin, A., Lemarié, F., Chelton, D., et al. (2016). Modulation of wind work by oceanic current interaction with the atmosphere. *Journal of Physical Oceanography*, *46*(6), 1685–1704. https://doi.org/10.1175/JPO-D-15-0232.1

Sasaki, Y., & Minobe, S. (2015). Climatological mean features and interannual to decadal variability of ring formations in the Kuroshio Extension region. *Journal of Oceanography*, *71*(5), 499–509. https://doi.org/10.1007/s10872-014-0270-4

Sasaki, Y., Minobe, S., & Schneider, N. (2013). Decadal response of the Kuroshio Extension jet to Rossby waves: Observation and thin-jet theory. *Journal of Physical Oceanography*, *43*(2), 442–456. https://doi.org/10.1175/JPO-D-12-096.1

Sasaki, Y., & Schneider, N. (2011). Decadal shifts of the Kuroshio Extension jet: Application of thin-jet theory. *Journal of Physical Oceanography*, *41*(5), 979–993. https://doi.org/10.1175/2010JPO4550.1

Scott, R., & Wang, F. (2005). Direct evidence of an oceanic inverse kinetic energy cascade from satellite altimetry. *Journal of Physical Oceanography*, *35*(9), 1650–1666. https://doi.org/10.1175/JPO2771.1

Smith, K. (2007). The geography of linear baroclinic instability in Earth's oceans. *Journal of Marine Research*, *65*(5), 655–683. https://doi.org/10.1357/002224007783649484

Smith, W., & Sandwell, D. (1997). Global seafloor topography from satellite altimetry and ship depth soundings. *Science*, *277*(5334), 1956–1962. https://doi.org/10.1126/science.277.5334.1956

Sugimoto, S., & Hanawa, K. (2009). Decadal and interdecadal variations of the Aleutian Low activity and their relation to upper oceanic variations over the North Pacific. *Journal of the Meteorological Society of Japan*, *87*, 601–614.

Sun, S., Wu, L., & Qiu, B. (2013). Response of the inertial recirculation to intensified stratification in a two-layer quasi-geostrophic ocean circulation model. *Journal of Physical Oceanography*, *43*(7), 1254–1269. https://doi.org/10.1175/JPO-D-12-0111.1

Taguchi, B., Qiu, B., Nonaka, M., Sasaki, H., Xie, S., & Schneider, N. (2010). Decadal variability of the Kuroshio Extension: Mesoscale eddies and recirculations. *Ocean Dynamics*, *60*(3), 673–691. https://doi.org/10.1007/s10236-010-0295-1

Taguchi, B., Xie, S., Mitsudera, H., & Kubokawa, A. (2005). Response of the Kuroshio Extension to Rossby waves associated with the 1970s climate regime shift in a high-resolution ocean model. *Journal of Climate*, *18*(15), 2979–2995. https://doi.org/10.1175/JCLI3449.1

Taguchi, B., Xie, S., Schneider, N., Nonaka, M., Sasaki, H., & Sasai, Y. (2007). Decadal variability of the Kuroshio Extension: Observations and an eddy-resolving model hindcast. *Journal of Climate*, *20*(11), 2357–2377. https://doi.org/10.1175/JCLI4142.1

Travis, S., & Qiu, B. (2017). Decadal variability in the South Pacific Subtropical Countercurrent and regional mesoscale eddy variability. *Journal of Physical Oceanography*, *47*(3), 499–512. https://doi.org/10.1175/JPO-D-16-0217.1

Wang, S., Liu, Z., & Pang, C. (2015). Geographical distribution and anisotropy of the inverse kinetic energy cascade, and its role in the eddy equilibrium processes. *Journal of Geophysical Research*, *120*, 4891–4906. https://doi.org/10.1002/2014JC010476

Waterman, S., Hogg, N., & Jayne, S. (2011). Eddy-mean interaction in the Kuroshio extension region. *Journal of Physical Oceanography*, *41*(6), 1182–1208. https://doi.org/10.1175/2010JPO4564.1

Waterman, S., & Hoskins, B. (2013). Eddy shape, orientation, propagation, and mean flow feedback in western boundary current jets. *Journal of Physical Oceanography*, *43*(8), 1666–1690. https://doi.org/10.1175/JPO-D-12-0152.1

Waterman, S., & Jayne, S. (2011). Eddy–mean flow interaction in the along-stream development of a western boundary current jet: An idealized model study. *Journal of Physical Oceanography*, *41*(4), 682–707. https://doi.org/10.1175/2010JPO4477.1

Wunsch, C., Heimbach, P., Ponte, R., Fukumori, I., & ECCO-Consortium members (2009). The global general circulation of the ocean estimated by the ECCO-Consortium. *Oceanography*, *22*, 88–103.

Yang, Y., & Liang, X. (2016). The instabilities and multiscaleenergetics underlying the mean–interannual–eddy interactions in the Kuroshio Extension region. *Journal of Physical Oceanography*, *46*(5), 1477–1494. https://doi.org/10.1175/JPO-D-15-0226.1

Yang, Y., Liang, X., Qiu, B., & Chen, S. (2017). On the decadal variability of the eddy kinetic energy in the Kuroshio Extension. *Journal of Physical Oceanography*, *47*(5), 1169–1187. https://doi.org/10.1175/JPO-D-16-0201.1